Seasonality and Predictability of the Indian Ocean Dipole Mode: ENSO Forcing and Internal Variability

YUN YANG,[*,+,#,@] SHANG-PING XIE,[*,+] LIXIN WU,[*] YU KOSAKA,[&] NGAR-CHEUNG LAU,[**,++] AND GABRIEL A. VECCHI[##]

[*] *Physical Oceanography Laboratory, Qingdao Collaborative Innovation Center of Marine Science and Technology, Ocean University of China, Qingdao, China*
[+] *Scripps Institution of Oceanography, University of California, San Diego, La Jolla, California*
[#] *College of Global Change and Earth System Science, Beijing Normal University, Beijing, China*
[@] *Joint Center for Global Studies, Beijing, China*
[&] *Research Center for Advanced Science and Technology, University of Tokyo, Tokyo, Japan*
[**] *Institute of Environment, Energy and Sustainability, Hong Kong, China*
[++] *Department of Geography and Resource Management, Chinese University of Hong Kong, Hong Kong, China*
[##] *National Oceanic and Atmospheric Administration/Geophysical Fluid Dynamics Laboratory, Princeton, New Jersey*

(Manuscript received 28 January 2015, in final form 19 May 2015)

ABSTRACT

This study evaluates the relative contributions to the Indian Ocean dipole (IOD) mode of interannual variability from the El Niño–Southern Oscillation (ENSO) forcing and ocean–atmosphere feedbacks internal to the Indian Ocean. The ENSO forcing and internal variability is extracted by conducting a 10-member coupled simulation for 1950–2012 where sea surface temperature (SST) is restored to the observed anomalies over the tropical Pacific but interactive with the atmosphere over the rest of the World Ocean. In these experiments, the ensemble mean is due to ENSO forcing and the intermember difference arises from internal variability of the climate system independent of ENSO. These elements contribute one-third and two-thirds of the total IOD variance, respectively. Both types of IOD variability develop into an east–west dipole pattern because of Bjerknes feedback and peak in September–November. The ENSO forced and internal IOD modes differ in several important ways. The forced IOD mode develops in August with a broad meridional pattern and eventually evolves into the Indian Ocean basin mode, while the internal IOD mode grows earlier in June, is more confined to the equator, and decays rapidly after October. The internal IOD mode is more skewed than the ENSO forced response. The destructive interference of ENSO forcing and internal variability can explain early terminating IOD events, referred to as IOD-like perturbations that fail to grow during boreal summer. The results have implications for predictability. Internal variability, as represented by preseason sea surface height anomalies off Sumatra, contributes to predictability considerably. Including this indicator of internal variability, together with ENSO, improves the predictability of IOD.

1. Introduction

The Indian Ocean dipole (IOD) is an east–west dipole mode of interannual variability over the tropical Indian Ocean (Saji et al. 1999; Webster et al. 1999). A positive IOD features an anomalous cooling off the coast of Sumatra/Java and a weak warming over the western tropical Indian Ocean. IOD is of great interest because of its influence on precipitation over the surrounding continents, Asian monsoon (Saji and Yamagata 2003b; Yamagata et al. 2004; Chang et al. 2006; Schott et al. 2009), and El Niño–Southern Oscillation (ENSO; Yu et al. 2002; Annamalai et al. 2005; Kug and Kang 2006; Kug et al. 2006; Luo et al. 2010; Izumo et al. 2010).

The debate over the triggers of IOD persists since the day the phenomenon was defined. Unlike the equatorial Pacific, the annual mean wind over the equatorial Indian Ocean is westerly, and the thermocline is relatively flat and deep without persistent equatorial upwelling. All these are unfavorable for the Bjerknes (1969) feedback that is fundamental to generating and maintaining ENSO variability. A number of studies attribute IOD variability to external forcing, particularly ENSO (e.g., Dommenget and Latif 2002; Baquero-Bernal et al. 2002;

Corresponding author address: Shang-Ping Xie, 9500 Gilman Drive, MC 206, La Jolla, CA 92093-0206.
E-mail: sxie@ucsd.edu

DOI: 10.1175/JCLI-D-15-0078.1

Li et al. 2003; Yu and Lau 2004). They considered anomalous alongshore winds off Sumatra/Java to be forced by the developing ENSO, which trigger the air–sea interaction over the Indian Ocean and lead to a mature IOD event in autumn. While IOD decays rapidly thereafter, ENSO continues to exert heat flux anomalies over the Indian Ocean, terminating and replacing IOD with the Indian Ocean basin (IOB) mode (Du et al. 2009). However, several intense IOD events took place without substantial ENSO forcing, such as in 1961 and 1994 (Saji et al. 1999; Yamagata et al. 2004; Luo et al. 2008a; Luo et al. 2010). These IOD events developed into the mature phase with coupled Bjerknes feedback (Saji et al. 1999; Yu and Rienecker 1999; Yamagata et al. 2004), suggesting the importance of internal variability. Other external forcing might also be responsible for the IOD formation, such as the southern annular mode (SAM; Lau and Nath 2004), Indo-Pacific warm pool (Annamalai et al. 2003; Song et al. 2007), and the Indonesian Throughflow (Tozuka et al. 2007). In this study, however, we focus on the ENSO forcing.

Numerous studies attempted to separate the contribution of ENSO forcing from internal (i.e., non-ENSO forced) variability. Some studies, based on observational data, conducted composite analysis, using pure IOD years to represent the internal IOD mode and IOD–ENSO co-occurring events to study the influence of ENSO (Yamagata et al. 2004; Song et al. 2007). The problem is that one cannot be sure the IOD variability is entirely forced by ENSO and has no contribution from internal variability in the IOD–ENSO co-occurring events. For instance, in Song et al. (2007), the triggers for the IOD–ENSO co-occurring composites sometimes appear in spring but other times in summer. Behera et al. (2006) found that ENSO forced and internal IOD modes develop in summer and spring, respectively. Therefore, the IOD–ENSO co-occurring events that develop in spring may be the joint effect of ENSO forcing and internal variability. Moreover, some modeling studies use regionally coupled experiments to study the impact of ENSO forcing on IOD (e.g., Behera et al. 2006; Huang and Shukla 2007b). The models, however, have their limitations in simulating ENSO, for instance, its amplitude and spatial structure (e.g., Lau and Nath 2000, 2003), which may cause the distortion of ENSO influence on IOD. To have a better simulation of ENSO forcing, Shinoda et al. (2004a) prescribed observed sea surface temperature (SST) over the tropical eastern Pacific while using slab ocean model over the rest of the ocean. This method successfully evaluated the impact of ENSO on IOD evolution via surface heat flux but excluded the potential mechanism of ocean dynamics. Using a fully coupled model, Huang and Shukla (2007a) restored the observed SST anomalies over the global ocean but let the Indian Ocean interact with the atmosphere. Kosaka et al. (2013) performed similar experiments to study summer variability over the Indo–northwestern Pacific, by restoring SST anomalies over the eastern and central equatorial Pacific (ECEP) to observations. They successfully extracted ENSO forcing and internal variability as the ensemble mean and intermember difference from their ensemble mean, respectively. In this study, we analyzed the same experiment as in Kosaka et al. (2013), but focusing on the IOD mode. Our experiment design is similar to Huang and Shukla (2007a), but we extend the study by a detailed comparison of ENSO forced and internal IOD modes and explore the implication for prediction.

Here, we adopt the method of Kosaka et al. (2013) to extract the forced and internal variability and to quantify the relative contribution. We find that the two IOD modes differ in seasonality, which may explain why some IOD events terminate early and fail to reach maturity. We show that the predictability of IOD can be improved significantly by considering internal variability. A benefit of prescribing observed ENSO over the ECEP is that we can compare the simulated IOD events with observations and infer the relative importance of ENSO forcing and internal variability for each event.

Early terminating IOD events, also known as aborted IOD events, are of great interest to researchers (Du et al. 2013). This type of IOD event develops in spring, matures in early summer, and rapidly decays afterward. Most studies (Gualdi et al. 2003; Rao and Yamagata 2004; Du et al. 2013) attribute this IOD termination to the Madden–Julian oscillation (MJO; Madden and Julian 1972), which generates westerlies and downwelling oceanic Kelvin waves that propagate toward Sumatra/Java and may kill a developing IOD event. In this paper, we suggest another explanation of this early termination as destructive interference between ENSO forced and internal IOD modes.

The rest of the paper is organized as follows. Section 2 introduces data and methods. Section 3 analyzes the mechanisms and skewness of the two IOD modes. Sections 4 and 5 study IOD predictability and the interference of the two IOD modes, respectively. Section 6 is a summary.

2. Data and methods

We use the Geophysical Fluid Dynamics Laboratory Climate Model, version 2.1 (GFDL CM2.1; Delworth et al. 2006). The atmosphere component is based on

the Atmospheric Model, version 2.1 (AM2.1), with 24 vertical levels and a horizontal resolution of 2.5° longitude × 2.0° latitude (Anderson et al. 2004). The ocean component is the Modular Ocean Model (MOM), version 4 (Griffies et al. 2003), which has 50 vertical layers and the resolution of 1.0° longitude × 1.0° latitude, with the meridional resolution equatorward of 30°S and 30°N becoming finer to ⅓° at the equator.

We use the Pacific Ocean–Global Atmosphere (POGA) experiment (Kosaka and Xie 2013), which consists of 10 runs started from 1 January 1940. The initial conditions for both the atmosphere and the ocean are taken from 10 historical runs started at 1861. The different initial conditions cause random differences in phase of natural variability among ensemble members. The results shown in this paper cover the period from 1950 to 2012, after a 10-yr spinup. In POGA, the radiative forcing is estimated from observations, including the atmospheric composition changes and the solar cycle. SST is prescribed as monthly SST climatology from long-term GFDL CM2.1 runs plus observed anomalies over the ECEP (15°S–15°N, 180°–coast), and is fully coupled to the atmosphere over the rest of the ocean. Following Rowell et al. (1995), the total variance can be decomposed into a forced component, related to the ensemble mean, and an internal component as a residual. In POGA, the ocean–atmosphere coupled system is forced by the observed variability over ECEP, much of which is due to ENSO. In this paper, we call this ECEP-triggered IOD variability the ENSO forced IOD mode while the residual is the internal IOD mode. We use the ensemble mean to indicate ENSO forcing and the deviation from the ensemble mean to represent the internal variability. In this study, we combine the 10 members together for the internal variability analysis to increase the sample size.

The POGA experiment simulates global temperature anomalies remarkably well, including the recent global warming hiatus (Kosaka and Xie 2013). It also successfully reproduces the Indian Ocean climatology, including the weak annual mean tropical westerlies, the flat and deep thermocline, and seasonal reversal of Asian monsoon (not shown). However, the thermocline off the coast of Sumatra/Java is shallower compared to the observed, which may lead to biases in IOD magnitude. Furthermore, POGA captures the interannual variability over the Indian Ocean, including IOD and IOB modes. POGA simulates a reasonable IOD structure, except for too strong westward extension of the eastern pole along the equator. The correlation between the leading principal component (PC1) of SST over the Indian Ocean (20°S–20°N, 40°–120°E) and the dipole mode index (DMI), defined as SST difference between (10°S–10°N, 50°–70°E) and (10°S–0°, 90°–110°E), reaches 0.97 in September–November (SON).

In this paper, we use the POGA experiment to study the ENSO forced and internal variability of IOD. Modeling studies provide a better way to separate the ENSO forcing and internal variability than the observations alone. However, models have biases in simulating ENSO and its global impact. By prescribing the observed SST anomalies over the ECEP, POGA uses observed ENSO variability to force the global ocean, which significantly reduces model biases and provides a reasonable method to evaluate the influence of ENSO on IOD. However, the POGA experiment has its own disadvantages. The energy is not conserved in POGA because of the prescribed SST anomalies. Moreover, ENSO and IOD are interactive, with strong IOD events exerting an influence on the evolution of ENSO (Luo et al. 2010; Izumo et al. 2010). POGA does not capture the IOD modulation on ENSO.

To verify model results, we use monthly mean observational SST from the Hadley Centre Sea Ice and Sea Surface Temperature (HadISST) dataset (Rayner et al. 2003) and Simple Ocean Data Assimilation (SODA), version 2.2.4 (Carton and Giese 2008). HadISST consists of data from 1870 to 2014, with a resolution of 1.0° longitude × 1.0° latitude. We choose the period of 1950–2012, the same as POGA. SODA covers the period of 1871–2008, with a resolution of 0.5° longitude × 0.5° latitude × 40 levels. We choose the period from 1948 to 2008.

3. ENSO forced and internal IOD mode

The POGA ensemble mean does an excellent job of reproducing Indian Ocean (20°S–20°N, 40°–120°E) annual mean SST, reaching a correlation of 0.93 with the HadISST (Fig. 1a). Here, we use December–February (DJF) Niño-3.4 index and SON DMI index to represent ENSO and IOD, respectively. The ENSO forced IOD variability, represented as the ensemble mean DMI, closely follows ENSO variation (correlation $r = 0.76$). The raw DMI for individual POGA realization correlates with the observed IOD only moderately at 0.45 (Fig. 1b, calculated as the mean correlation of each individual run). The correlation between ENSO and IOD in observations is also moderate at 0.57. These moderate correlations indicate that the ENSO forcing alone cannot fully explain IOD variability and imply the importance of internal variability. We use raw, ensemble mean and intermember difference of DMI variance to indicate total, ENSO forced, and internal variance of IOD in POGA. ENSO forced variability, with a variance of 0.24°C^2, explains only one-third of total variance

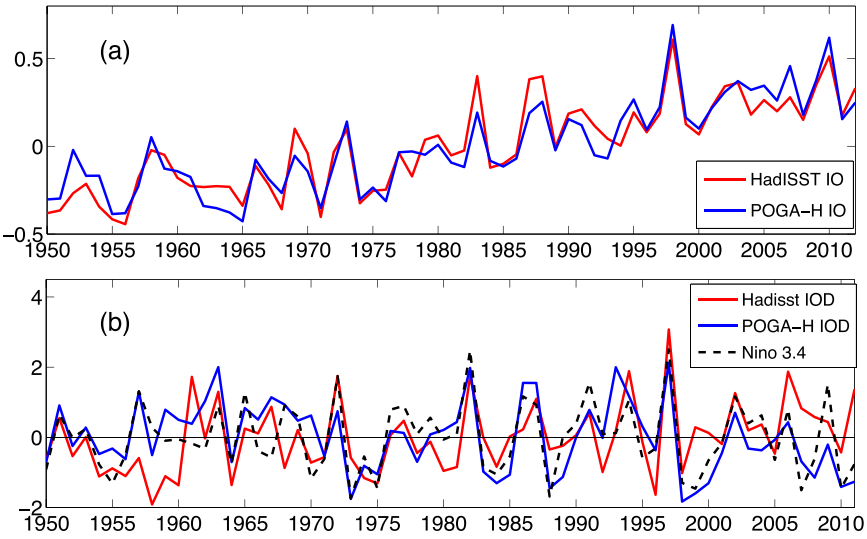

FIG. 1. (a) Annual mean SST anomaly (°C) time series averaged over the tropical IOB (20°S–20°N, 40°–120°E), and (b) SON DMI index, defined as SST difference between (10°S–10°N, 50°–70°E) and (10°S–0°, 90°–110°E). DJF Niño-3.4 (5°S–5°N, 120°–170°W) SST is also shown in the bottom panel as a dashed curve. DMI and Niño-3.4 indexes are standardized.

($0.67°C^2$), leaving the other two-thirds ($0.43°C^2$) to internal variability. After removing the ENSO forcing, the internal IOD shows a marginal peak around 3–4 years (Fig. 2). The ENSO forced IOD, by contrast, features a significant spectral peak at 5 years, consistent with ENSO.

During the past 63 years, some strong IOD events are followed by ENSO while others are independent of ENSO. This intermittent relationship is simulated well in the POGA experiment. The ensemble mean captures some strong IOD events that coexist with strong ENSO events, such as in 1982 and 1997 (Fig. 1b). These are the IOD events forced by ENSO. Some other strong IOD events in observations, however, are missing from the POGA ensemble mean, and they do not co-occur with strong ENSO events, for instance, in 1961, 1994, and 2006 (e.g., Luo et al. 2010). These events are likely due to internal variability. Therefore, both ENSO forced and internal variability are important in the development of IOD events.

a. Evolution of IOD modes

To study the evolution of ENSO forced and internal IOD modes, seasonal empirical orthogonal function (SEOF) analysis is performed. SEOF is based on conventional empirical orthogonal function analysis, but the eigenvector represents seasonally evolving spatial patterns that share the same principal component (Wang and An 2005). In this study, we use monthly rather than seasonal data. To focus on the IOD mode, we apply SEOF to equatorial (5°S–5°N, 40°–120°E) thermocline depth anomalies because IOB barely involves ocean dynamics in this region.

The two types of IOD modes share similarities. They both start to develop with coherent wind anomalies off Sumatra/Java (Figs. 3b,c). The alongshore wind anomalies shoal the thermocline depth (Z20, 20°C isothermal depth) (Figs. 4b,c), bring cold water to surface, and lead to SST cooling. The cold SST anomalies strengthen zonal SST gradient and the southeasterly winds. The anomalies begin to grow because of this positive feedback of Bjerknes (1969), consistent with previous studies (e.g., Li et al. 2003). When reaching their peak phases in boreal autumn (SON), the two IOD modes feature a typical east–west dipole pattern with a stronger eastern pole in both SST and thermocline depth (Figs. 3e,f and 4e,f), consistent with observations (Saji and Yamagata 2003a). Meanwhile, wind anomalies feature strong southeasterlies along the Indonesian coast and easterlies on the equator, forming a pair of anticyclonic wind curls and deepening of the thermocline on either side of the equator (Fig. 4). These thermocline depth anomalies, however, fail to cause SST warming over the western south Indian Ocean (SIO) because of the opposing effect of heat flux anomalies (Figs. 3a–h). During the developing and mature stages, the heat flux acts as a reinforcing effect off the equator but a damping effect on the equator.

The ENSO forced and internal IOD modes differ in many ways. For the internal IOD, SST evolves into a dipole pattern, especially for the western pole, in June (Fig. 3b) while the forced IOD starts to develop 2 months

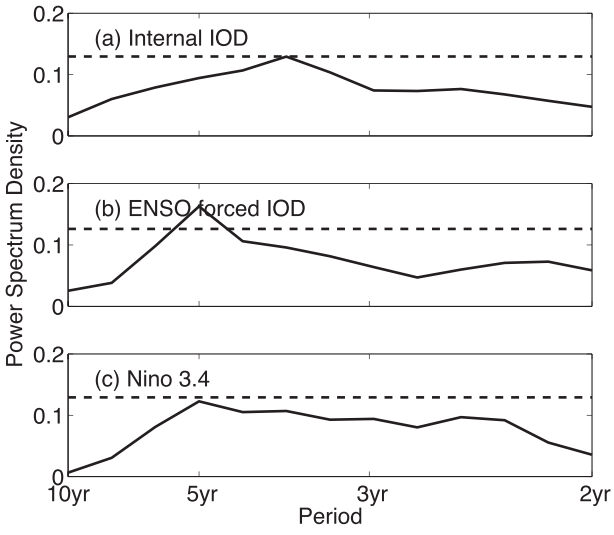

FIG. 2. Power spectra of DMI associated with (a) internal IOD and (b) ENSO forced IOD, and (c) Niño-3.4 SST in DJF. Unit is year. Dashed line illustrates 95% significance level, evaluated against white noise. The power spectra of internal IOD mode is calculated by each individual run and then make the average, and that of the forced IOD mode is calculated using ensemble mean DMI index.

later in August (Fig. 3c). Moreover, the wind anomalies off Sumatra/Java and over the central equatorial Indian Ocean for the internal IOD appear 2 months earlier than for the forced IOD. This difference can also be seen in the latitudinal mean results (Fig. 6b versus Fig. 6d) that the warm western pool and wind anomalies appear in June for the internal IOD but in August for the forced IOD. This late development of the forced IOD is due to the late emergence of alongshore wind anomalies, in response to the growth of ENSO that peaks in December.

Figure 5 shows the internal, forced (magnified by 2) and observed (magnified by 3) IOD variance in calendar months. The internal variability starts to increase in June while the forced IOD remains flat until August (Fig. 5a). The observed IOD, involving both IOD modes, starts to develop from May/June. The standardized variance of the internal IOD exceeds that of the forced IOD in spring and summer (Fig. 5b), which further demonstrates the discrepancy in the timing of evolution. This discrepancy largely agrees with Shinoda et al. (2004a), although different methods are used.

Moreover, the forced IOD mode has a much broader meridional spatial pattern while the internal mode is more confined to the equator (Chakravorty et al. 2014; Fig. 3). This difference is due to the broad influence of ENSO on the Indian Ocean while the Bjerknes feedback is confined to the equator, which limits the spatial extent of the internal IOD mode. Specifically, both IOD modes show northwesterly wind anomalies that reach 30°S in October over the southern subtropical Indian Ocean (Figs. 3e,f). The wind anomalies keep growing in the forced mode and lead to local SST warming by counteracting the climatological wind (Fig. 3g). In contrast, those wind anomalies dissipate in the internal mode and fail to form a strong warming (Fig. 3h). In the Northern Hemisphere, the strong easterly anomalies in the forced mode cover the northern tropical Indian Ocean and extend to 15°N (Fig. 3e), but those in the internal mode are much weaker, with little signal north of 10°N (Fig. 3f). The anomalous wind stress curl associated with these easterlies is strong over the northern Arabian Sea and the Bay of Bengal in the forced IOD mode, in contrast to that in the internal mode (Figs. 4e,f).

In addition, the forced IOD has stronger SST anomalies over the western pole, consistent with previous studies (e.g., Behera et al. 2006). The dynamics are different on versus off the equator. The warmer north Indian Ocean in the forced IOD is partially due to the stronger heat flux anomalies, especially latent heat flux (Figs. 3e,f). The broad easterly anomalies forced by ENSO weaken the prevailing monsoon westerlies and lead to SST warming in the following month (Fig. 3g). In addition, the anomalous wind curls over the northern Indian Ocean in the forced mode deepen the thermocline (Figs. 4e,g) and thereby increase SST. In the western equatorial Indian Ocean, the positive SST anomalies are attributed to anomalous ocean heat transport by ocean current, in response to enhanced zonal gradient of sea level pressure forced by the ENSO (Drbohlav et al. 2007). This is in conflict with some previous studies that El Niño tends to warm the western Indian Ocean by modifying surface heat flux (Shinoda et al. 2004a,b; Zhong et al. 2005; Behera et al. 2006). This disagreement might be due to the overly active coupled IOD in POGA, with an overly strong SST response (Fig. 5a). The latent heat flux can be treated as a mixture of atmospheric forcing and SST response acting as Newtonian cooling (Xie et al. 2010). The overestimation of SST anomalies can lead to a stronger Newtonian cooling and make the total latent heat flux a damping effect on the SST anomalies, even with a positive effect of atmospheric forcing. Furthermore, the internal IOD decays rapidly after October while the forced IOD mode eventually evolves into the basin warming pattern (Figs. 3i–l), consistent with previous studies (e.g., Shinoda et al. 2004b). Our model has a bias in simulating the IOB mode, with anomalous cooling over the northern equatorial Indian Ocean in spring.

To summarize IOD dynamics, we examine the time–latitude evolution over the equator (5°S–5°N, 40°–120°E). For the internal mode, the alongshore wind anomalies emerge in May (not shown) and grow in June, concurrent

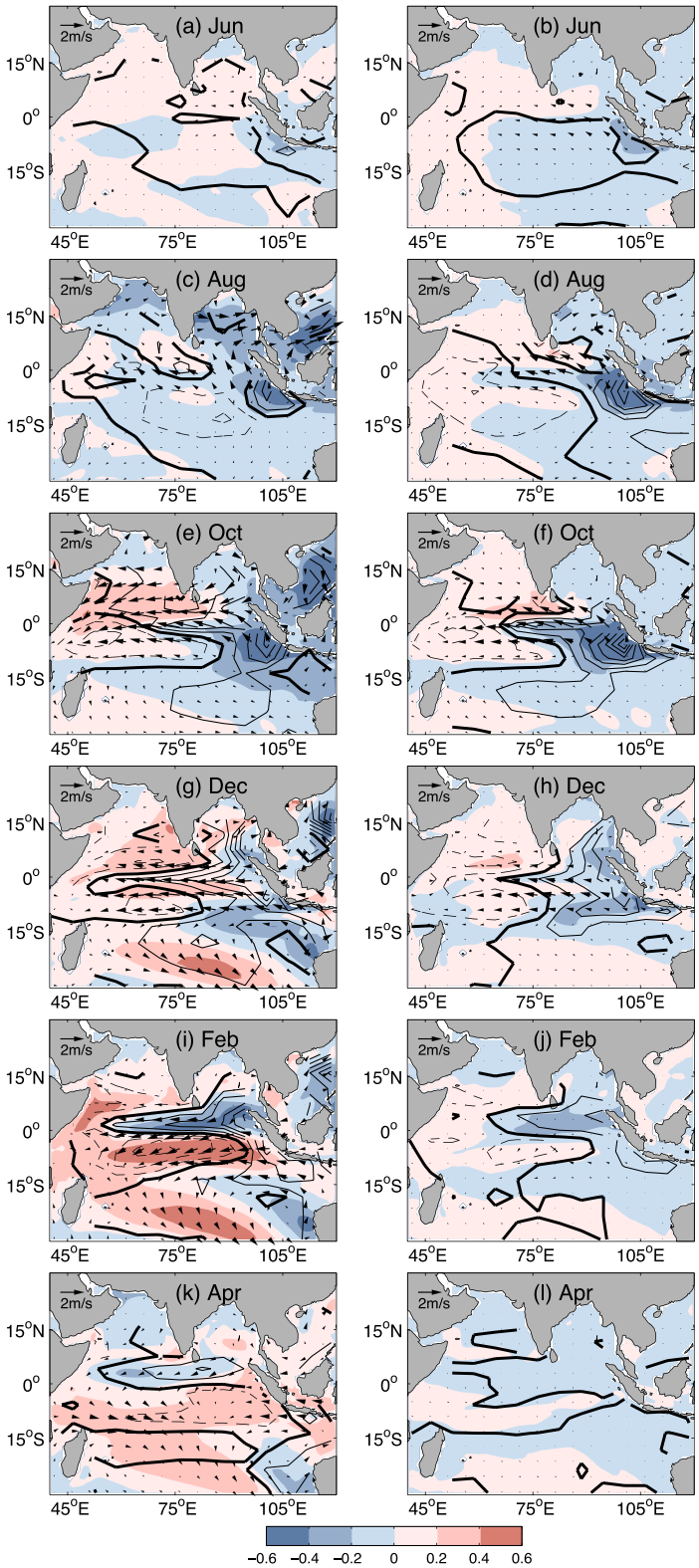

FIG. 3. Regressed anomalies of SST (°C, color shading), wind ($m\,s^{-1}$, vector), and surface heat flux ($W\,m^{-2}$, contours, solid to warm the ocean) against PC1 for (left) ENSO forced and (right) internal variability in POGA.

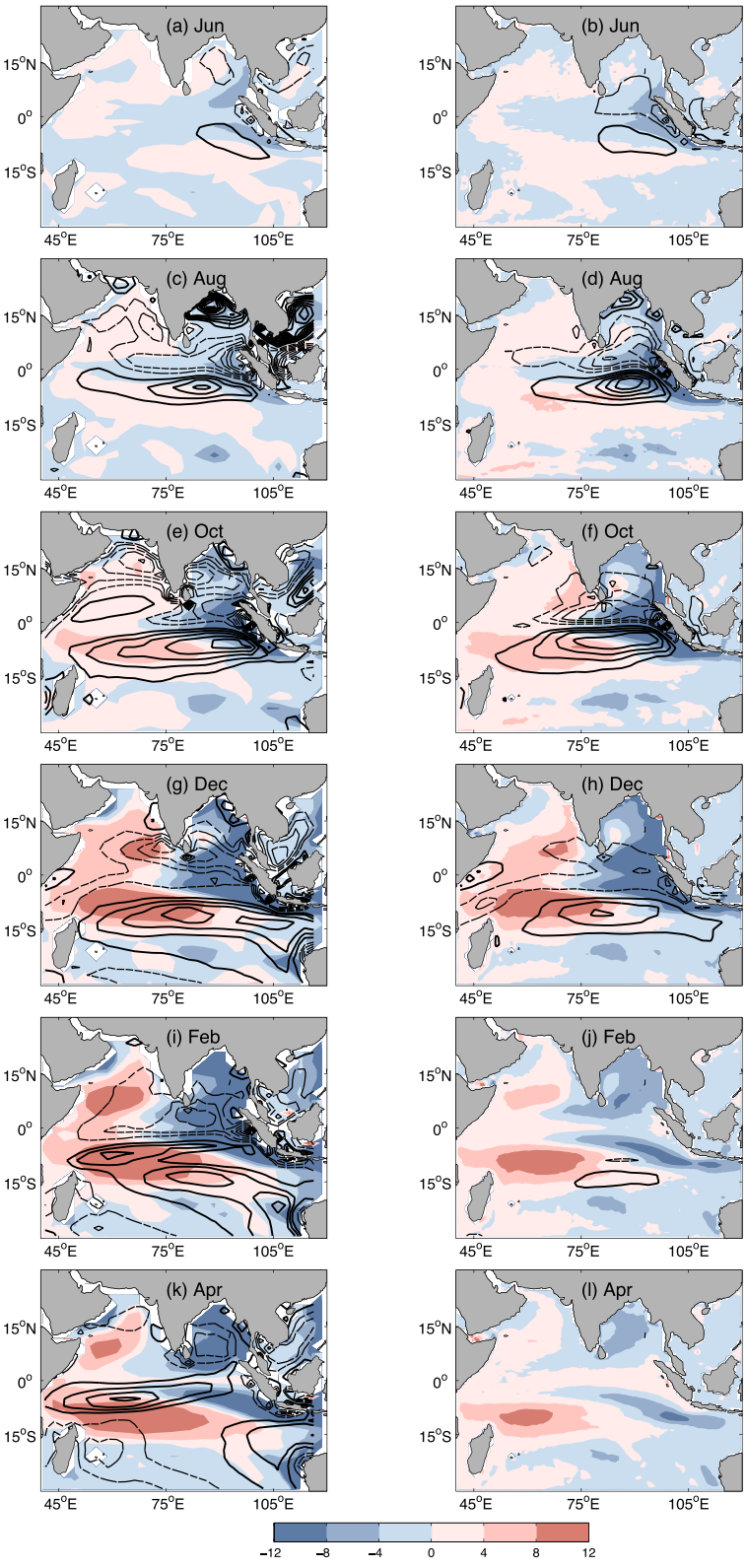

FIG. 4. As in Fig. 3, but for Z20 (m, color shading) and wind curl (10^{-8} N m^{-3}, contours) anomalies.

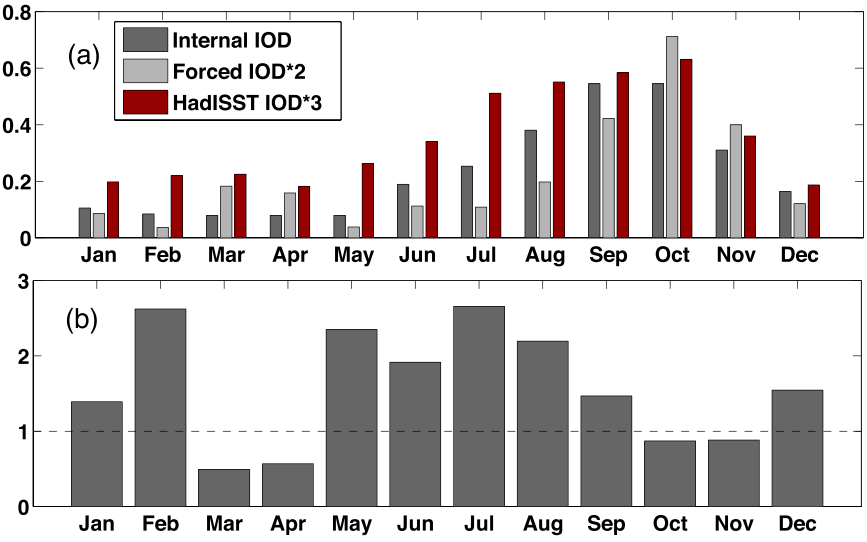

FIG. 5. (a) Internal, ENSO forced (magnified by 2), and HadISST (magnified by 3) DMI variance in calendar months, and (b) ratio of internal to ENSO forced DMI variance (the internal and forced variance is normalized by individual annual standard deviation before calculating their ratio).

with the onset of the summer monsoon (Fig. 6f). In response, the thermocline shoals and SST drops (Figs. 6d,e). The ENSO forced IOD mode develops by a similar mechanism but 2 months later, because of the late appearance of alongshore wind anomalies (Figs. 6a–c). The internal mode has a weaker western pole but a stronger eastern pole (Figs. 6b,e). The differences between the two IOD modes are significant in the following year. After October, the anomalous SST and thermocline depth anomalies of the internal mode decay rapidly with the alongshore wind anomalies, but the weak dipole pattern after December can persist until the following March (Figs. 6d–f). The wind anomalies forced by ENSO, however, turn into easterlies after December and persist until the following March. These anomalous easterlies weaken background wind and warm SST, evolving into the IOB mode (Figs. 6b,c).

The western SIO is the region with the shallowest thermocline over the Indian Ocean (not shown) and strong influence of thermocline variability on SST (Xie et al. 2002). In the internal IOD, an anticyclonic wind curl appears in June (Fig. 7f) in the eastern basin, associated with the anomalous equatorial easterlies. This wind curl induces an anomalous Ekman downwelling and a deepening of the thermocline, which copropagate toward the west as Rossby waves (e.g., Chakravorty et al. 2014; Figs. 7d,f). The forced IOD shares similar dynamics, but appears 2 months later in August and features stronger wind curl anomalies as well as larger thermocline depth anomalies (Figs. 7a,c versus Figs. 7d,f). The thermocline anomalies in the internal mode gradually dissipate with wind curl after December (Fig. 7d). The anomalous thermocline depth in the forced mode, by contrast, remains strong even in the following April (cf. the 40-m contour between Figs. 7a and 7d) because of the persistent wind curl anomalies. SSTs in both IOD modes feature strong cooling over the eastern basin, in response to the alongshore wind anomalies (Figs. 7b,e). Over the western SIO, the heat flux anomalies offset the thermocline-deepening effect, leading to a weak SST warming for both IOD modes (Fig. 3). In the following spring, these heat flux anomalies dissipate rapidly with the dipole pattern while the thermocline anomalies remain robust because of the strong wind curl forcing, allowing SST anomalies to stay in response to the thermocline deepening in the forced mode (Figs. 7a,b). For the internal mode, however, SST anomalies weaken after December because of the rapid dissipation of wind stress curl (Figs. 7d–f). The positive SST anomalies in the western SIO, albeit weak, persist through June–August, riding on the westward propagating downwelling Rossby waves (Figs. 7d,e). In the POGA experiment, the anomalous thermocline displacements are centered at similar latitudes for both forced and internal IOD modes at around 6°–10°S (Fig. 4), unlike what was found in previous studies (Yu et al. 2005).

b. *IOD skewness*

The observed IOD features a strong asymmetry toward positive phase (Hong et al. 2008; Zheng et al. 2010; Ogata et al. 2013). This asymmetry can be seen from both ENSO forcing and internal IOD modes: the positive IOD

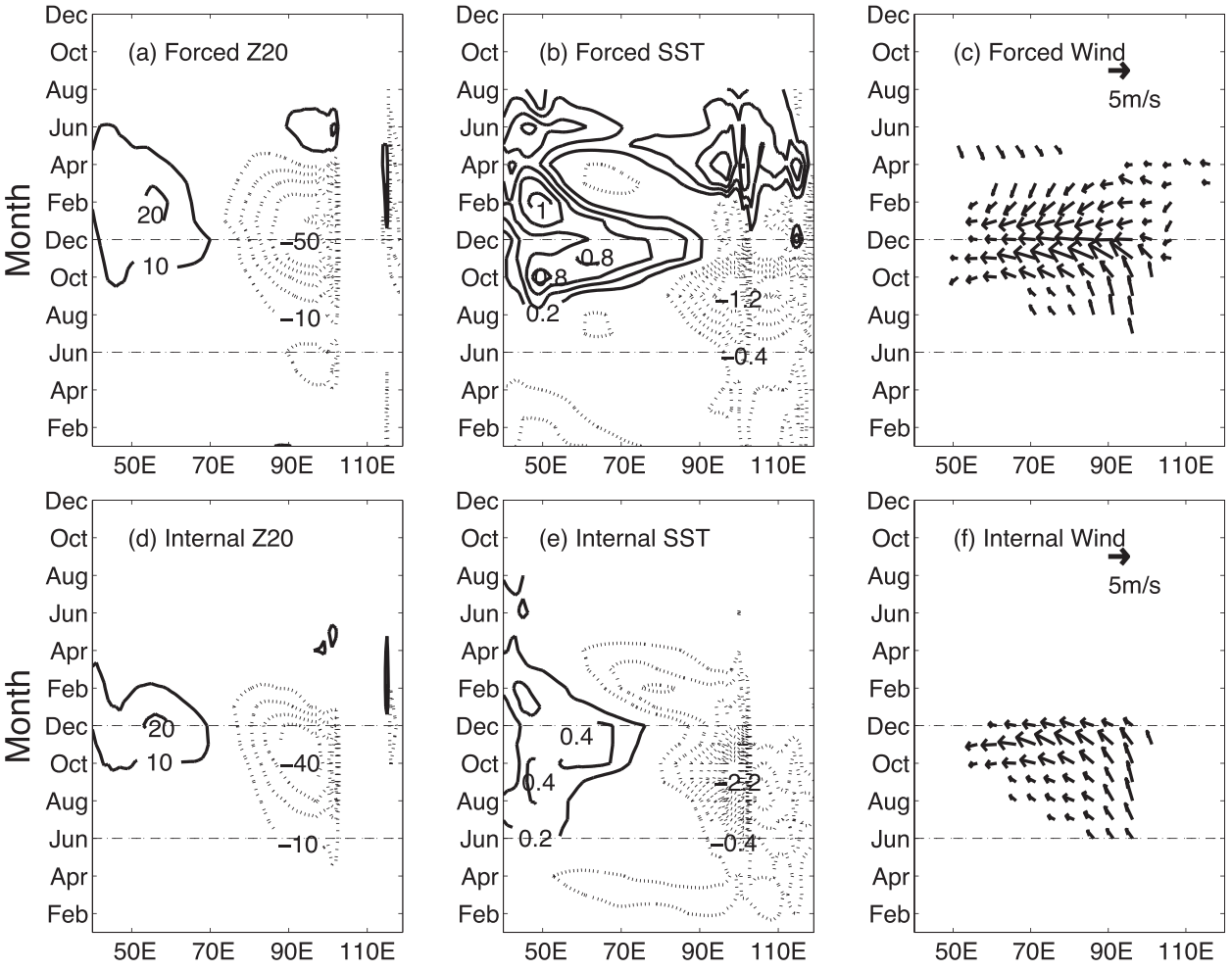

FIG. 6. Lagged composite anomalies of (a),(d) Z20 (m); (b),(e) SST (°C); and (c),(f) wind (m s^{-1}, only points with velocity larger than 1.5 m s^{-1} are displayed), averaged over 5°S–5°N for Z20 and SST, and over 8°S–0° for wind, as a function of longitude and calendar month for (top) ENSO forced and (bottom) internal IOD modes in POGA. Composites are obtained for SEOF PC1 $> 1\sigma$.

features a larger magnitude and a greater number of extreme events ($>2\sigma$; with σ denoting standard deviation; Table 1). In addition, the asymmetry grows with the magnitude of IOD events. Specifically, the two phases show a comparable number of strong IOD events ($>1\sigma$), but positive phase outnumbers in extreme events. Particularly, the internal IOD has 10 positive super extreme events ($>3\sigma$) but none in the negative phase.

To measure the asymmetry amplitude, we calculate the skewness of IOD, following An and Jin (2004):

$$\text{Skewness} = \frac{m_3}{(m_2)^{3/2}},$$

where m_k is the kth moment,

$$m_k = \sum_{i=1}^{N} \frac{(x_i - \overline{X})^k}{N};$$

x_i is the ith datum, $\overline{X}$ is the climatological mean, and N is the length of data. The statistical significance of skewness is estimated as follows:

$$\frac{\text{skewness}}{\sqrt{6N(N-1)/(N-2)(N+1)(N+3)}} = n(1),$$

where $n(1)$ is the normal distribution and $n(1) = 1.64$ at the 90% level.

The raw IOD variability in POGA shows a strong positive skewness (0.83; Table 2). The internal IOD is markedly skewed at 0.95 while the skewness of forced IOD is modest at 0.38, comparable to that of ENSO (0.34). The skewness for both IOD modes increases rapidly with the increasing IOD magnitude. Take the forced IOD as an example: the skewness is −0.33 for moderate IOD events ($<1\sigma$), it increases to 0.36 for strong IOD events ($>1\sigma$), and it reaches 1 for extremes ($>2\sigma$).

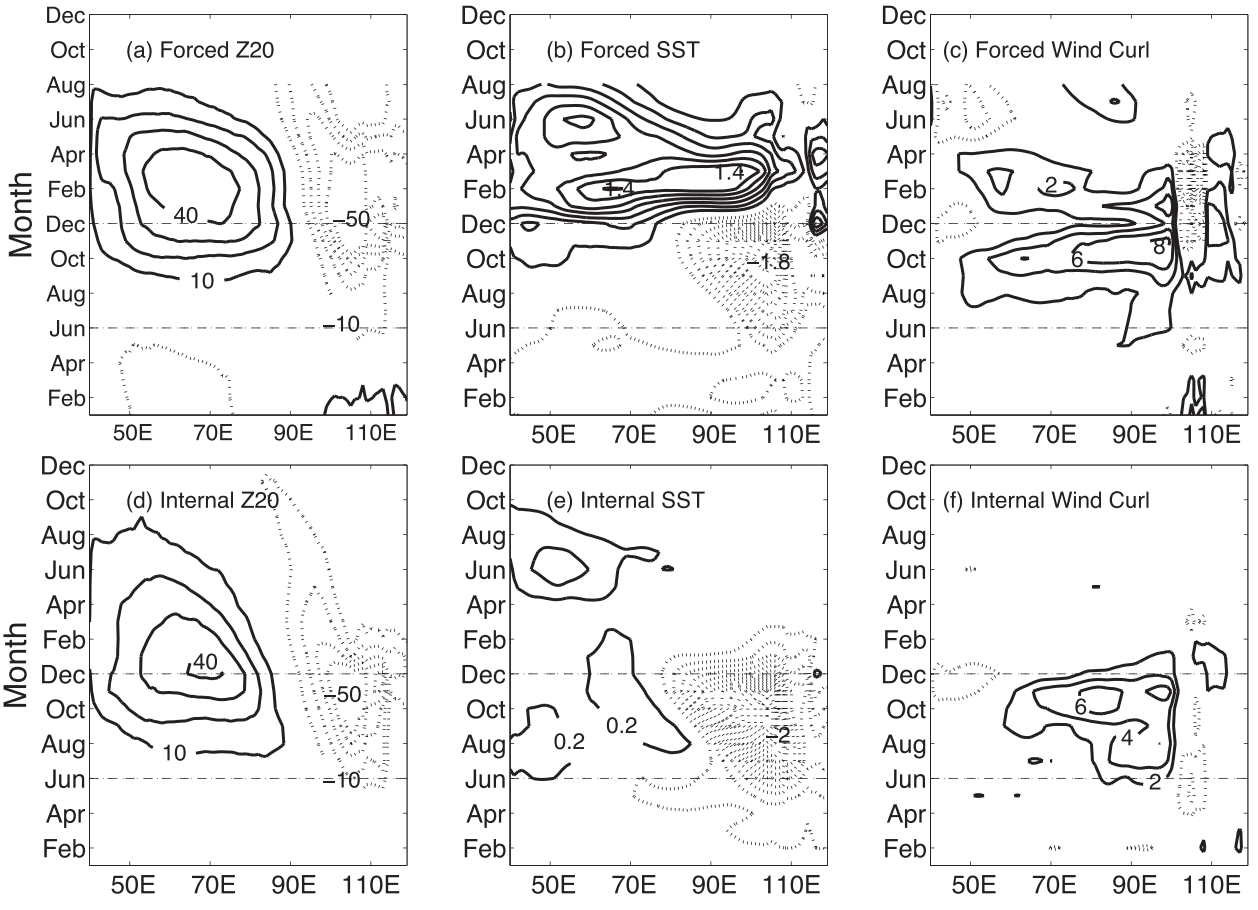

FIG. 7. As in Fig. 6, but averaged over 6°—10°S, and (c),(f) for wind curl (10^{-8} N m^{-3}).

One group of studies attributes the skewness to the ocean, and especially to the depth of the thermocline over the eastern equatorial Indian Ocean (EEIO; 10°S–0°, 90°–110°E) (Ogata et al. 2013; Cai and Qiu 2013). The EEIO thermocline shoals (deepens) in positive (negative) IOD phase (Fig. 8), but only negative subsurface temperature anomalies extend to the surface to initiate air–sea interaction for the IOD growth. Take internal IOD, for instance: the ocean temperature anomalies in positive phase, centered at 75-m depth, extend all the way to the surface and cool the SST by 1.3°C (Fig. 8c). By contrast, the negative IOD events feature a maximum warming around 100 m with a weak SST effect of 0.8°C (Fig. 8d). To test this theory, we examine the relationship between sea surface height (SSH) anomalies (SSHAs) and SST anomaly over the EEIO (Figs. 9a,b), because SSHA is a good indicator of thermocline depth anomalies. The two indices show a positive correlation. This correlation, however, is nonlinear, with SST more sensitive to the shoaling than deepening of the thermocline. For instance, SST in the internal mode

TABLE 1. Number of IOD events in POGA. Positive and negative events in which DMI exceeds 1σ, 2σ, and 3σ thresholds are counted for internal and ENSO forced IOD.

	Internal IOD		ENSO forced IOD	
	Positive	Negative	Positive	Negative
1σ	80	68	7	6
2σ	27	3	4	0
3σ	10	0	0	0

TABLE 2. Skewness of IOD and ENSO. IOD skewness is evaluated based on DMI in POGA. For ENSO, Niño-3.4 SST is used for POGA and HadISST data. Italic denotes skewness not passing 99% significance level.

IOD type	Internal	ENSO forced	Raw series
IOD	0.95	*0.38*	0.83
IOD (<1σ)	*−0.41*	*−0.33*	*−0.58*
IOD (>1σ)	0.71	*0.36*	−0.74
IOD (>2σ)	0.98	1.00	1.00
IOD (>3σ)	1.00		1.00
ENSO			*0.34*
HadISST IOD			0.61

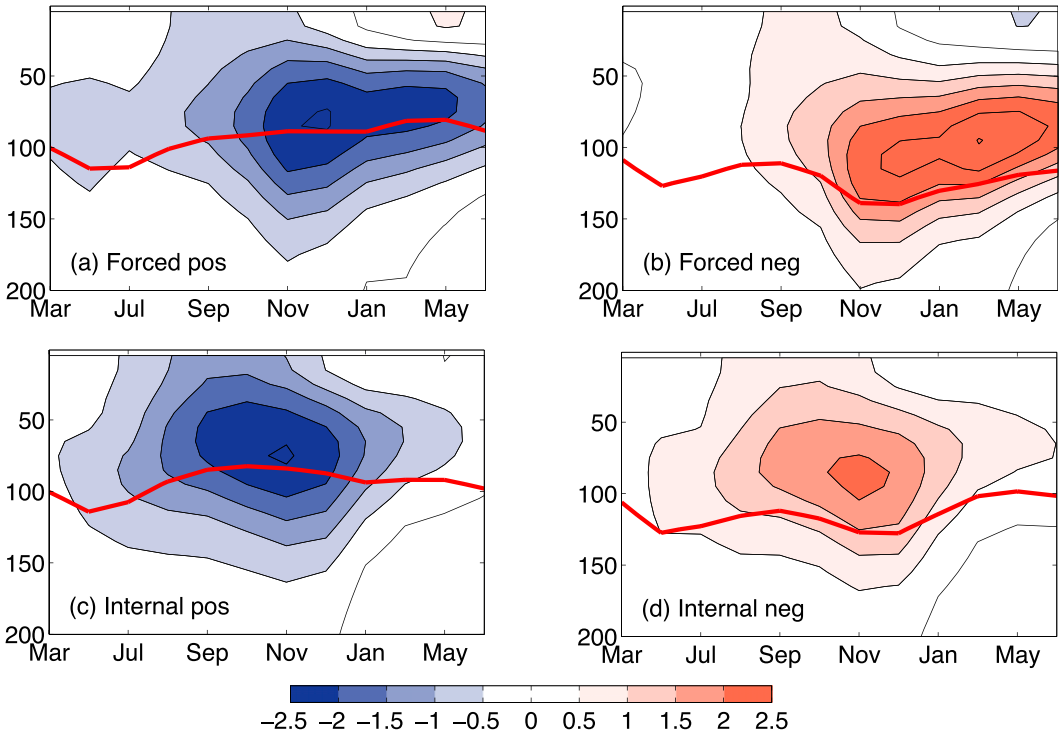

FIG. 8. Time–depth section of Z20 (m, red contour) and temperature anomalies (°C, color shading) over EEIO (10°S–0°, 90°–110°E) composited for SEOF PC1 exceeding (left) $+1\sigma$ and (right) -1σ for (top) forced and (bottom) internal IOD modes.

cools for 1.7°C while it warms only 1.2°C in response to 0.1-m variation of SSH. Hong et al. (2008), however, argues the importance of the atmosphere for IOD skewness. In POGA experiment, the net heat flux anomalies are in a linear relationship with SSTA and do not contribute to the IOD skewness (not shown). The cloud effect is also nonlinear. However, it tends to damp the SST anomalies and weaken the skewness of IOD (Figs. 9c,d), with shortwave radiation damping negative SSTA more than positive anomalies. These results indicate that the ocean dynamics are responsible for the IOD asymmetry.

4. Implications for predictability

IOD prediction using dynamical models shows promising skills, but the skill and lead time need to be improved compared to ENSO prediction. The ENSO effect on IOD can be predicted several months in advance (Wajsowicz 2005; Luo et al. 2007; Song et al. 2008; Shi et al. 2012), but the predictability of internal IOD is not as good (Hendon and Wang 2009) except for the extreme events (Luo et al. 2008a, 2010). We use a new index to include internal variability—the EEIO SSHA—because the dynamical state is well captured by SSHA and EEIO is the origin as well as a center of action for IOD. ENSO can be predicted with skill two seasons in advance (Luo et al. 2008b). In this paper, we assume that the Niño-3.4 index can be predicted with perfect skill after spring and examine the effect of internal IOD variability on prediction, by using October Niño-3.4 to represent a perfect prediction of ENSO. Specifically, we predict SON IOD using preseason EEIO SSHA and October Niño 3.4: $\mathrm{DMI}_{\mathrm{SON}} = a\mathrm{ENSO}_{\mathrm{Oct}} + b\mathrm{SSHA}_{\mathrm{month}}$.

Figure 10 shows the correlation between POGA simulated and our predicted SON DMI. The prediction is significant at the 99% level (correlation $r = 0.38$; calculated from t test, with degrees of freedom adjusted by the autocorrelation of each time series). In POGA, the correlation between SON DMI and October Niño-3.4 SST is 0.49, which is not an excellent prediction. By adding EEIO SSHA as the second predictor, the predictability improves remarkably. The ensemble mean correlation with the bipredictor scheme increases to 0.65 for June initialization. This improvement indicates the great influence of internal variability on IOD prediction. The internal IOD itself contributes significant predictability after May initialization, and this contribution increases rapidly with longer lead time. To verify the POGA result, we performed the same analysis using

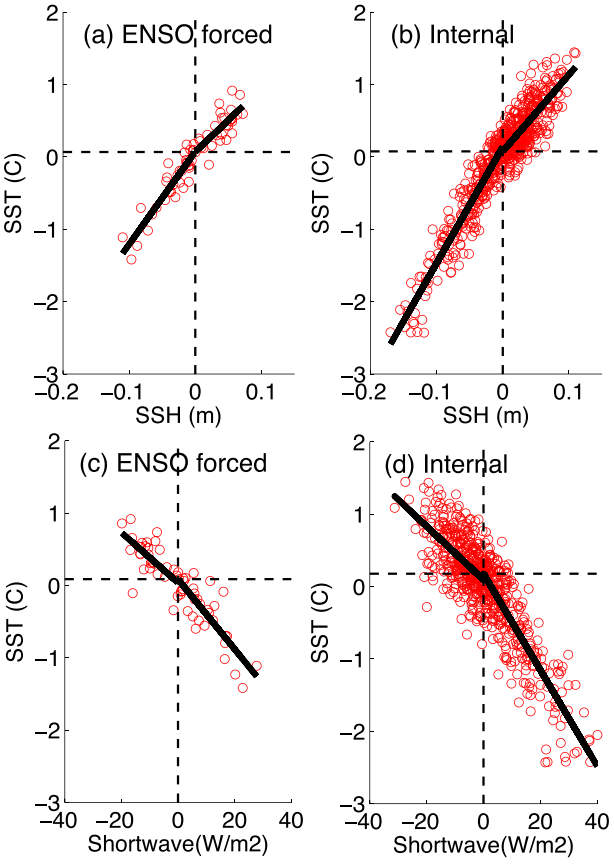

FIG. 9. Scatterplots of SSH (m) and SST (°C) anomalies over EEIO: (a) ENSO forced and (b) internal variability in POGA. (c),(d) As in (a),(b), but for surface downward shortwave (W m^{-2}) and SST anomalies. Solid black lines denote the linear regressions obtained separately for positive and negative anomalies of x axis.

SODA data. The contribution of preseason EEIO SSHA is clear with slightly lower correlation than in POGA (Fig. 10). These results suggest that the POGA experiment may overestimate the internal variability. One should notice that the SODA SSHA here includes the effect of ENSO, because we cannot have it removed entirely in the real world. However, the improvement of the black solid line over the black diamond still demonstrates the contribution of internal variability.

The SSHA we used here is raw data instead of intermember difference from ensemble mean, because one cannot entirely remove ENSO forcing in the observed data. The predictability calculated from intermember difference (not shown) is similar to Fig. 10 but with slightly lower correlation. Although the raw SSHA involves influence from ENSO, it successfully includes the internal variability in predicting SON DMI. Moreover, the SSHA before summer is dominated by internal variability due to the late development of the forced IOD mode.

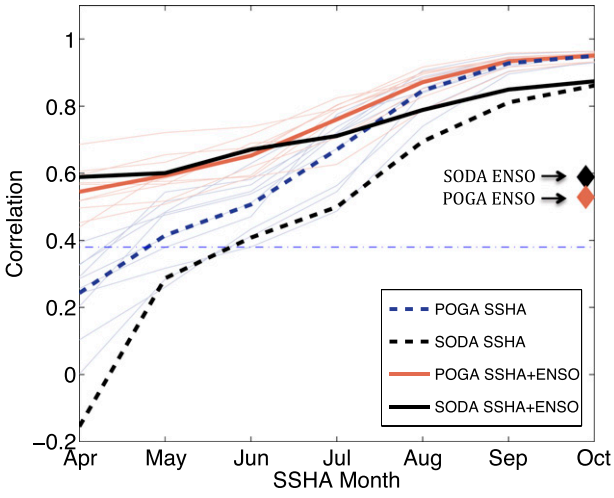

FIG. 10. Correlation of the SON DMI with the EEIO SSHA index (dashed), October Niño-3.4 SST index (presented as diamonds), and these two indexes together (solid). The thin and thick lines demonstrate results of 10 ensembles and ensemble mean, respectively. The blue dashed line denotes 99% significant level. The x axis represents the month of EEIO SSHA initialization.

5. Interference of ENSO forced and internal IOD

The development of individual IOD may be viewed as a result of the interference of ENSO forced and internal variability. Internal IOD develops in spring and early summer, but not all the internal IOD events can eventually develop into mature IOD in SON. Instead some of them decay and terminate before autumn. Previous studies attribute such early terminating IOD events, also known as aborted IOD events, as a consequence of interference by atmospheric intraseasonal variability, the MJO (Gualdi et al. 2003; Rao and Yamagata 2004; Du et al. 2013). Here, we suggest another possibility: a positive (negative) internal IOD event that has developed in spring is weakened by the opposing effect of La Niña (El Niño) in summer. Behera et al. (2006) examined such a damping effect of ENSO on IOD. We define an early terminating IOD as a significant internal IOD event in June (magnitude of June EEIO SSHA $> 1\sigma$) that fails to develop into strong SON IOD (DMI $> 1\sigma$) of the same sign.

Figure 11 shows the SON IOD index (colored for sign and magnitude) with various initial internal IOD conditions in June (EEIO SSHA) and ENSO forcing (Niño-3.4 in October). All three indexes are standardized. If internal IOD and ENSO forcing reinforce each other (upper-left and lower-right quadrants in Fig. 11), there tend to be strong IOD events in SON, especially when both factors are large. The termination rate is low when EEIO SSHA is positive (negative) in La Niña (El Niño) years (Fig. 12). Strong events are rare when the two

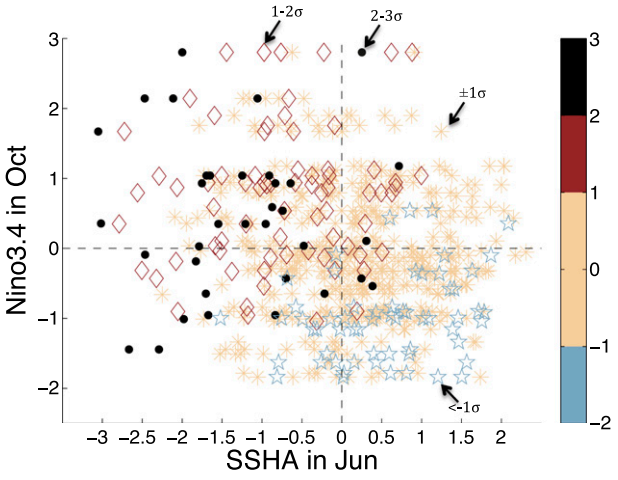

FIG. 11. Scatterplots of SON DMI index (color scatters) for various magnitudes of EEIO SSHA in June (x axis) and ENSO forcing in October (Niño-3.4 SST; y axis) in POGA. The DMI, SSHA, and Niño 3.4 SST indexes are all standardized. IOD modes with magnitude of 2σ–3σ, 1σ–2σ, within $\pm1\sigma$, and $<-1\sigma$ are indicated as black dots, red diamonds, yellow stars, and blue pentacles, respectively.

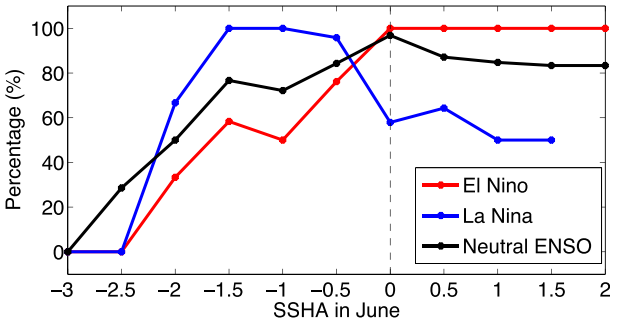

FIG. 12. Percentage (number of early terminating IOD events divided by total IOD events that happened in each ENSO phase) of early terminating IOD events in POGA as a function of standardized EEIO SSHA in June, under different ENSO phases. El Niño, neutral ENSO, and La Niña years are defined as DJF Niño-3.4 SST anomaly $>1\sigma$, within $\pm1\sigma$, and $<-1\sigma$, respectively.

factors act to oppose each other (upper-right and lower-left quadrants in Fig. 11). Most positive IOD events are terminated by La Niña when June SSHA is moderate between −2 and 0 (Fig. 12). Correspondingly, all negative IOD events in June are terminated or even turned into strong positive events by the developing El Niño. This asymmetry in termination rate may be due to stronger El Niño than La Niña, which decreases the chance of early terminating positive IOD and further contributes to the positive skewness of IOD (Cai et al. 2012). When ENSO is neutral ($<1\sigma$), the termination rate is dependent on IOD initial amplitude, decreasing with increasing IOD amplitude (Fig. 12). Moreover, the internal variability seems to have a stronger influence on IOD than ENSO, with the lower-left quadrant in Fig. 11 having more positive than negative IOD events. The termination rate vanishes when internal IOD is super strong (SSHA < -2.5), further demonstrating the leading effect of internal variability (Fig. 12).

To further illustrate how ENSO forcing and internal variability interfere with each other and contribute to IOD development, 1961 and 1997 IOD events are chosen as representatives of internal and ENSO forced positive IOD events, respectively. Figure 13 shows 10 simulations of IOD evolution in 1961 and 1997. The year 1961 is a weak La Niña year; the IOD evolution in this year is probably due to the internal mode. Among the 10 simulations, there are two strong negative events and two strong positive events, with the positive events of greater magnitude. This is consistent with the skewness of IOD. The year 1997, however, has the strongest El Niño documented in history. In spring and early summer, the simulations show a broad spread of IOD magnitude, indicating the uncertainty due to internal variability. El Niño exerts its influence after August, forcing DMI to increase. Nine out of 10 simulations evolve into strong IOD events in SON. Specifically, some simulations develop positive (negative) IOD events in spring, which are enhanced (reversed sign) by ENSO forcing. Some start neutral and grow in summer under ENSO forcing. In one simulation, a negative IOD event develops in June but weakens after August, probably because of El Niño forcing. This is an early terminating negative IOD event.

6. Summary

The development of IOD is due to both ENSO forcing and internal variability. To distinguish these two factors, a POGA experiment is performed. In this experiment, SST is restored to the observed anomalies over the ECEP but interactive with the atmosphere elsewhere. Ten simulations are performed over the period of 1950–2012. We use the ensemble mean and intermember difference to represent ENSO forcing and internal IOD variability. The POGA experiment captures the main characteristics of IOD. The comparison of the ensemble mean with observations indicates that the 1982 and 1997 IOD events are forced by ENSO while the1961 and 1994 events are due to internal variability. In POGA, the internal component contributes two-thirds of total variance and plays a more important role in IOD variability. ENSO forced IOD is responsible for the remaining one-third of variance.

We extract IOD evolution by performing monthly SEOF of equatorial thermocline depth variability. The

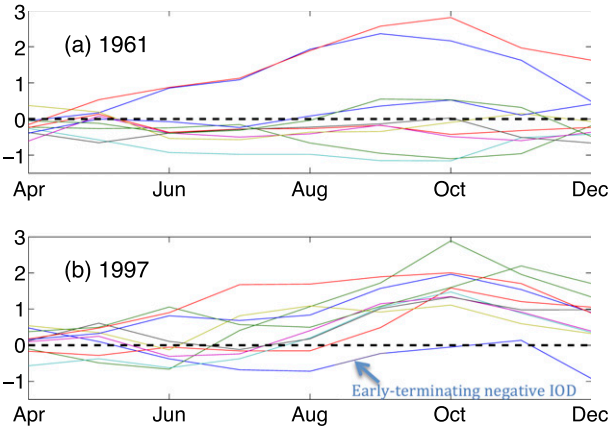

FIG. 13. DMI evolutions in10 simulations of POGA in (a) 1961 and (b) 1997.

two modes of IOD both develop into a zonal dipole pattern with the help of the Bjerknes feedback and reach the mature phase in SON. Therefore, the growing mechanism for IOD evolution lies in the Indian Ocean. The two types of IOD modes differ in evolution. The internal IOD starts to develop in June when the Asian monsoon sets up the upwelling-favorable alongshore southeasterlies off Sumatra, while the forced IOD waits another 2 months for ENSO forcing. The internal IOD is confined to near the equator where the Bjerknes feedback operates, while forced IOD has a broader meridional pattern because of the broad influence of ENSO. The forced IOD eventually evolves into the IOB mode while internal IOD decays rapidly after October.

An important characteristic of the IOD is the asymmetry between positive and negative phases. This asymmetry can be seen in both types of IOD modes, but that of the internal variability is much stronger. This positive skewness is due to the stronger sensitivity of SST to thermocline shoaling than deepening. The skewness increases with the amplitude of IOD, a result that applies to both IOD modes. Cai et al. (2014) suggests that there will be more extreme IOD events in the future because of global warming, and we expect most of them to be positive events. In response, the severe droughts and floods due to extreme positive events might also be more frequent in the future.

Including the internal IOD mode helps improve the IOD predictability and explains why some IOD-like perturbations do not grow. We propose a new index—the preseason EEIO SSHA—to represent the internal variability. Initializing with this internal IOD index in May or after improves the IOD predictability in combination with ENSO. The contribution of internal variability to IOD predictability is supported by an observational analysis using SODA, illustrating the utility of decomposing IOD variability into forced and internal components. In SODA, internal variability is weaker and ENSO forcing is relatively more important. Shi et al. (2012) reached a similar conclusion that internal variability contributes significantly to the IOD predictability, although using different models, methods, and the predicted Niño-3.4 index. They also pointed out that the highest skill for IOD prediction lies in the western SIO, associated with the forced Rossby wave. The predictability of EEIO SSHA is lower than that of ENSO, limiting the predictability of IOD (Hendon and Wang 2009).

The ENSO forcing and internal variability sometimes work constructively to form a strong IOD event, but sometimes work destructively to diminish the IOD activity. This provides an explanation of early terminating IOD events: an internal positive (negative) IOD perturbation that develops in spring may be terminated in summer by the opposing forcing of La Niña (El Niño).

Although POGA simulates IOD reasonably well, the biases are still present. Particularly, POGA simulates too shallow a thermocline over the EEIO. This bias leads to the unrealistically strong IOD variance ($0.67°C^2$), which is 4 times of the observed value ($0.15°C^2$). This large amplitude bias is common among CMIP5 models (Cai and Cowan 2013; Liu et al. 2014; Li et al. 2015). In addition, our model simulates a stronger skewness (0.83) of IOD than the observed (0.61). The too shallow thermocline in EEIO may cause the overestimation of the internal effect on IOD predictability by exaggerating the internal variability.

Acknowledgments. This work is supported by the National Basic Research Program of China (2012CB955600), the China National Natural Science Foundation (NSFC) Key Project (41130859), NSFC Creative Group Project (40921004), the U.S. National Science Foundation, a scholarship from the Chinese Scholarship Council to Yun Yang (201306330025), and the Ministry of Education, Culture, Sports, Science and Technology (MEXT) of Japan through Grant-in-Aid for Young Scientists to Yu Kosaka (15H05466).

REFERENCES

An, S.-I., and F.-F. Jin, 2004: Nonlinearity and asymmetry of ENSO. *J. Climate*, **17**, 2399–2412, doi:10.1175/1520-0442(2004)017<2399:NAAOE>2.0.CO;2.

Anderson, J. L., and Coauthors, 2004: The new GFDL global atmosphere and land model AM2–LM2: Evaluation with prescribed SST simulations. *J. Climate*, **17**, 4641–4673, doi:10.1175/JCLI-3223.1.

Annamalai, H., R. Murtugudde, J. Potemra, S.-P. Xie, P. Liu, and B. Wang, 2003: Coupled dynamics over the Indian Ocean:

Spring initiation of the zonal mode. *Deep-Sea Res. II*, **50**, 2305–2330, doi:10.1016/S0967-0645(03)00058-4.

——, S.-P. Xie, J. P. McCreary, and R. Murtugudde, 2005: Impact of Indian Ocean sea surface temperature on developing El Niño. *J. Climate*, **18**, 302–319, doi:10.1175/JCLI-3268.1.

Baquero-Bernal, A., M. Latif, and S. Legutke, 2002: On dipolelike variability in the tropical Indian Ocean. *J. Climate*, **15**, 1358–1368, doi:10.1175/1520-0442(2002)015<1358:ODVOSS>2.0.CO;2.

Behera, S. K., J. J. Luo, S. Masson, S. A. Rao, H. Sakuma, and T. Yamagata, 2006: A CGCM study on the interaction between IOD and ENSO. *J. Climate*, **19**, 1688–1705, doi:10.1175/JCLI3797.1.

Bjerknes, J., 1969: Atmospheric teleconnections from the equatorial Pacific. *Mon. Wea. Rev.*, **97**, 163–172, doi:10.1175/1520-0493(1969)097<0163:ATFTEP>2.3.CO;2.

Cai, W., and T. Cowan, 2013: Why is the amplitude of the Indian Ocean Dipole overly large in CMIP3 and CMIP5 climate models? *Geophys. Res. Lett.*, **40**, 1200–1205, doi:10.1002/grl.50208.

——, and Y. Qiu, 2013: An observation-based assessment of nonlinear feedback processes associated with the Indian Ocean dipole. *J. Climate*, **26**, 2880–2890, doi:10.1175/JCLI-D-12-00483.1.

——, P. van Rensch, T. Cowan, and H. H. Hendon, 2012: An asymmetry in the IOD and ENSO teleconnection pathway and its impact on Australian climate. *J. Climate*, **25**, 6318–6329, doi:10.1175/JCLI-D-11-00501.1.

——, A. Santoso, G. Wang, E. Weller, L. Wu, K. Ashok, Y. Masumoto, and T. Yamagata, 2014: Increased frequency of extreme Indian Ocean Dipole events due to greenhouse warming. *Nature*, **510**, 254–258, doi:10.1038/nature13327.

Carton, J. A., and B. S. Giese, 2008: A reanalysis of ocean climate using Simple Ocean Data Assimilation (SODA). *Mon. Wea. Rev.*, **136**, 2999–3017, doi:10.1175/2007MWR1978.1.

Chakravorty, S., C. Gnanaseelan, J. S. Chowdary, and J.-J. Luo, 2014: Relative role of El Niño and IOD forcing on the southern tropical Indian Ocean Rossby waves. *J. Geophys. Res. Oceans*, **119**, 5105–5122, doi:10.1002/2013JC009713.

Chang, P., and Coauthors, 2006: Climate fluctuations of tropical coupled system—The role of ocean dynamics. *J. Climate*, **19**, 5122–5174, doi:10.1175/JCLI3903.1.

Delworth, T. L., and Coauthors, 2006: GFDL's CM2 global coupled climate models. Part I: Formulation and simulation characteristics. *J. Climate*, **19**, 643–674, doi:10.1175/JCLI3629.1.

Dommenget, D., and M. Latif, 2002: A cautionary note on the interpretation of EOFs. *J. Climate*, **15**, 216–225, doi:10.1175/1520-0442(2002)015<0216:ACNOTI>2.0.CO;2.

Drbohlav, H.-K. L., S. Gualdi, and A. Navarra, 2007: A diagnostic study of the Indian Ocean dipole mode in El Niño and non–El Niño years. *J. Climate*, **20**, 2961–2977, doi:10.1175/JCLI4153.1.

Du, Y., S.-P. Xie, K. Hu, and G. Huang, 2009: Role of air–sea interaction in the long persistence of El Niño–induced North Indian Ocean warming. *J. Climate*, **22**, 2023–2038, doi:10.1175/2008JCLI2590.1.

——, W. Cai, and Y. Wu, 2013: A new type of the Indian Ocean dipole since the mid-1970s. *J. Climate*, **26**, 959–972, doi:10.1175/JCLI-D-12-00047.1.

Griffies, S., M. J. Harrison, R. C. Pacanowski, and A. Rosati, 2003: A technical guide to MOM4. GFDL Ocean Group Tech. Rep. 5, NOAA/Geophysical Fluid Dynamics Laboratory, Princeton, NJ, 295 pp.

Gualdi, S., E. Guilyardi, A. Navarra, S. Masina, and P. Delecluse, 2003: The interannual variability in the Indian Ocean as simulated by a CGCM. *Climate Dyn.*, **20**, 567–582.

Hendon, H. H., and G. Wang, 2009: Seasonal prediction of the Leeuwin Current using the POAMA dynamical seasonal forecast model. *Climate Dyn.*, **34**, 1129–1137, doi:10.1007/s00382-009-0570-3.

Hong, C.-C., T. Li, LinHo, and J.-S. Kug, 2008: Asymmetry of the Indian Ocean dipole. Part I: Observational analysis. *J. Climate*, **21**, 4834–4848, doi:10.1175/2008JCLI2222.1.

Huang, B., and J. Shukla, 2007a: Mechanisms for the interannual variability in the tropical Indian Ocean. Part I: The role of remote forcing from the tropical Pacific. *J. Climate*, **20**, 2917–2936, doi:10.1175/JCLI4151.1.

——, and ——, 2007b: Mechanisms for the interannual variability in the tropical Indian Ocean. Part II: Regional processes. *J. Climate*, **20**, 2937–2960, doi:10.1175/JCLI4169.1.

Izumo, T., and Coauthors, 2010: Influence of the state of the Indian Ocean dipole on the following year's El Niño. *Nat. Geosci.*, **3**, 168–172, doi:10.1038/ngeo760.

Kosaka, Y., and S.-P. Xie, 2013: Recent global-warming hiatus tied to equatorial Pacific surface cooling. *Nature*, **501**, 403–407, doi:10.1038/nature12534.

——, ——, N.-C. Lau, and G. A. Vecchi, 2013: Origin of seasonal predictability for summer climate over the northwestern Pacific. *Proc. Natl. Acad. Sci. USA*, **110**, 7574–7579, doi:10.1073/pnas.1215582110.

Kug, J.-S., and I.-S. Kang, 2006: Interactive feedback between the Indian Ocean and ENSO. *J. Climate*, **19**, 1784–1801, doi:10.1175/JCLI3660.1.

——, T. Li, S.-I. An, I.-S. Kang, J.-J. Luo, S. Masson, and T. Yamagata, 2006: Role of the ENSO–Indian Ocean coupling on ENSO variability in a coupled GCM. *Geophys. Res. Lett.*, **33**, L09710, doi:10.1029/2005GL024916.

Lau, N.-C., and M. J. Nath, 2000: Impact of ENSO on the variability of the Asian–Australian monsoons as simulated in GCM experiments. *J. Climate*, **13**, 4287–4309, doi:10.1175/1520-0442(2000)013<4287:IOEOTV>2.0.CO;2.

——, and ——, 2003: Atmosphere–ocean variations in the Indo-Pacific sector during ENSO episodes. *J. Climate*, **16**, 3–20, doi:10.1175/1520-0442(2003)016<0003:AOVITI>2.0.CO;2.

——, and ——, 2004: Coupled GCM simulation of atmosphere–ocean variability associated with zonally asymmetric SST changes in the tropical Indian Ocean. *J. Climate*, **17**, 245–265, doi:10.1175/1520-0442(2004)017<0245:CGSOAV>2.0.CO;2.

Li, G., S.-P. Xie, and Y. Du, 2015: Monsoon-induced biases of climate models over the tropical Indian Ocean. *J. Climate*, **28**, 3058–3072, doi:10.1175/JCLI-D-14-00740.1.

Li, T., B. Wang, C.-P. Chang, and Y. S. Zhang, 2003: A theory for the Indian Ocean dipole–zonal mode. *J. Atmos. Sci.*, **60**, 2119–2135, doi:10.1175/1520-0469(2003)060<2119:ATFTIO>2.0.CO;2.

Liu, L., S.-P. Xie, X.-T. Zheng, T. Li, Y. Du, G. Huang, and W.-D. Yu, 2014: Indian Ocean variability in the CMIP5 multi-model ensemble: The zonal dipole mode. *Climate Dyn.*, **43**, 1715–1730, doi:10.1007/s00382-013-2000-9.

Luo, J.-J., S. Masson, S. Behera, and T. Yamagata, 2007: Experimental forecasts of the Indian Ocean dipole using a coupled OAGCM. *J. Climate*, **20**, 2178–2190, doi:10.1175/JCLI4132.1.

——, S. Behera, Y. Masumoto, H. Sakuma, and T. Yamagata, 2008a: Successful prediction of the consecutive IOD in 2006 and 2007. *Geophys. Res. Lett.*, **35**, L14S02, doi:10.1029/2007GL032793.

——, S. Masson, S. K. Behera, and T. Yamagata, 2008b: Extended ENSO predictions using a fully coupled ocean–atmosphere model. *J. Climate*, **21**, 84–93, doi:10.1175/2007JCLI1412.1.

——, R. Zhang, S. K. Behera, Y. Masumoto, F.-F. Jin, R. Lukas, and T. Yamagata, 2010: Interaction between El Niño and extreme

Indian Ocean dipole. *J. Climate*, **23**, 726–742, doi:10.1175/2009JCLI3104.1.

Madden, R. A., and P. R. Julian, 1972: Description of global-scale circulation cells in tropics with a 40–50 day period. *J. Atmos. Sci.*, **29**, 1109–1123, doi:10.1175/1520-0469(1972)029<1109:DOGSCC>2.0.CO;2.

Ogata, T., S.-P. Xie, J. Lan, and X. Zheng, 2013: Importance of ocean dynamics for the skewness of the Indian Ocean dipole mode. *J. Climate*, **26**, 2145–2159, doi:10.1175/JCLI-D-11-00615.1.

Rao, S. A., and T. Yamagata, 2004: Abrupt termination of Indian Ocean dipole events in response to intraseasonal disturbances. *Geophys. Res. Lett.*, **31**, L19306, doi:10.1029/2004GL020842.

Rayner, N. A., D. E. Parker, E. B. Horton, C. K. Folland, L. V. Alexander, D. P. Rowell, E. C. Kent, and A. Kaplan, 2003: Global analyses of sea surface temperature, sea ice, and night marine air temperature since the late nineteenth century. *J. Geophys. Res.*, **108**, 4407, doi:10.1029/2002JD002670.

Rowell, D. P., C. K. Folland, K. Maskell, and M. N. Ward, 1995: Variability of summer rainfall over tropical North Africa (1906–92): Observations and modelling. *Quart. J. Roy. Meteor. Soc.*, **121**, 669–704, doi:10.1002/qj.49712152311.

Saji, N. H., and T. Yamagata, 2003a: Structure of SST and surface wind variability during Indian Ocean dipole mode events: COADS observations. *J. Climate*, **16**, 2735–2751, doi:10.1175/1520-0442(2003)016<2735:SOSASW>2.0.CO;2.

——, and ——, 2003b: Possible impacts of Indian Ocean Dipole mode event on global climate. *Climate Res.*, **25**, 151–169, doi:10.3354/cr025151.

——, B. N. Goswami, P. N. Vinayachandran, and T. Yamagata, 1999: A dipole mode in the tropical Indian Ocean. *Nature*, **401**, 360–363.

Schott, F. A., S.-P. Xie, and J. P. McCreary, 2009: Indian Ocean circulation and climate variability. *Rev. Geophys.*, **47**, RG1002, doi:10.1029/2007RG000245.

Shi, L., H. H. Hendon, O. Alves, J.-J. Luo, M. Balmaseda, and D. Anderson, 2012: How predictable is the Indian Ocean dipole? *Mon. Wea. Rev.*, **140**, 3867–3884, doi:10.1175/MWR-D-12-00001.1.

Shinoda, T., M. A. Alexander, and H. H. Hendon, 2004a: Remote response of the Indian Ocean to interannual SST variations in the tropical Pacific. *J. Climate*, **17**, 362–372, doi:10.1175/1520-0442(2004)017<0362:RROTIO>2.0.CO;2.

——, H. H. Hendon, and M. A. Alexander, 2004b: Surface and subsurface dipole variability in the Indian Ocean and its relation to ENSO. *Deep-Sea Res. I*, **51**, 619–635, doi:10.1016/j.dsr.2004.01.005.

Song, Q., G. A. Vecchi, and A. J. Rosati, 2007: Indian Ocean variability in the GFDL CM2 coupled climate model. *J. Climate*, **20**, 2895–2916, doi:10.1175/JCLI4159.1.

——, ——, and ——, 2008: Predictability of the Indian Ocean sea surface temperature anomalies in the GFDL coupled model. *Geophys. Res. Lett.*, **35**, L02701, doi:10.1029/2007GL031966.

Tozuka, T., J.-J. Luo, S. Masson, and T. Yamagata, 2007: Decadal modulations of the Indian Ocean dipole in the SINTEX-F1 coupled GCM. *J. Climate*, **20**, 2881–2894, doi:10.1175/JCLI4168.1.

Wajsowicz, R. C., 2005: Potential predictability of tropical Indian Ocean SST anomalies. *Geophys. Res. Lett.*, **32**, L24702, doi:10.1029/2005GL024169.

Wang, B., and S.-I. An, 2005: A method for detecting season-dependent modes of climate variability: S-EOF analysis. *Geophys. Res. Lett.*, **32**, L15710, doi:10.1029/2005GL022709.

Webster, P. J., A. M. Moore, J. P. Loschnigg, and R. R. Leben, 1999: Coupled ocean–atmosphere dynamics in the Indian Ocean during 1997–98. *Nature*, **401**, 356–360, doi:10.1038/43848.

Xie, S.-P., H. Annamalai, F. A. Schott, and J. P. McCreary, 2002: Structure and mechanisms of South Indian Ocean climate variability. *J. Climate*, **15**, 864–878, doi:10.1175/1520-0442(2002)015<0864:SAMOSI>2.0.CO;2.

——, C. Deser, G. A. Vecchi, J. Ma, H. Teng, and A. T. Wittenberg, 2010: Global warming pattern formation: Sea surface temperature and rainfall. *J. Climate*, **23**, 966–986, doi:10.1175/2009JCLI3329.1.

Yamagata, T., S. K. Behera, J.-J. Luo, S. Masson, M. Jury, and S. A. Rao, 2004: Coupled ocean–atmosphere variability in the tropical Indian Ocean. *Earth Climate: The Ocean–Atmosphere Interaction*, *Geophys. Monogr.*, Vol. 147, Amer. Geophys. Union, 189–212.

Yu, J.-Y., and K. M. Lau, 2004: Contrasting Indian Ocean SST variability with and without ENSO influence: A coupled atmosphere-ocean GCM study. *Meteor. Atmos. Phys.*, **90**, 179–191, doi:10.1007/s00703-004-0094-7.

——, C. R. Mechoso, J. C. McWilliams, and A. Arakawa, 2002: Impacts of the Indian Ocean on the ENSO cycle. *Geophys. Res. Lett.*, **29**, 1204, doi:10.1029/2001GL014098.

Yu, L. S., and M. M. Rienecker, 1999: Mechanisms for the Indian Ocean warming during the 1997–98 El Niño. *Geophys. Res. Lett.*, **26**, 735–738, doi:10.1029/1999GL900072.

Yu, W., B. Xiang, L. Liu, and N. Liu, 2005: Understanding the origins of interannual thermocline variations in the tropical Indian Ocean. *Geophys. Res. Lett.*, **32**, L24706, doi:10.1029/2005GL024327.

Zheng, X.-T., S.-P. Xie, G. A. Vecchi, Q. Liu, and J. Hafner, 2010: Indian Ocean dipole response to global warming: Analysis of ocean–atmospheric feedbacks in a coupled model. *J. Climate*, **23**, 1240–1253, doi:10.1175/2009JCLI3326.1.

Zhong, A., H. H. Hendon, and O. Alves, 2005: Indian Ocean variability and its association with ENSO in a global coupled model. *J. Climate*, **18**, 3634–3649, doi:10.1175/JCLI3493.1.